Geophysical Research Letters

The Spatiotemporal Evolution of Granular Microslip Precursors to Laboratory Earthquakes

Daniel T. Trugman[1] , Ian W. McBrearty[2], David C. Bolton[3] , Robert A. Guyer[4,5] , Chris Marone[3,6] , and Paul A. Johnson[4]

[1]Department of Geological Sciences, Jackson School of Geosciences, The University of Texas at Austin, Austin, TX, USA, [2]Department of Geophysics, Stanford University, Stanford, CA, USA, [3]Department of Geosciences, Pennsylvania State University, University Park, PA, USA, [4]Geophysics Group, Earth and Environmental Sciences Division, Los Alamos National Laboratory, Los Alamos, NM, USA, [5]Department of Physics, University of Nevada, Reno, Reno, NV, USA, [6]Dipartimento Scienze della Terra, Sapienza Universitá di Roma, Rome, Italy

Abstract Laboratory earthquake experiments provide important observational constraints for our understanding of earthquake physics. Here we leverage continuous waveform data from a network of piezoceramic sensors to study the spatial and temporal evolution of microslip activity during a shear experiment with synthetic fault gouge. We combine machine learning techniques with ray theoretical seismology to detect, associate, and locate tens of thousands of microslip events within the gouge layer. Microslip activity is concentrated near the center of the system but is highly variable in space and time. While microslip activity rate increases as failure approaches, the spatiotemporal evolution can differ substantially between stick-slip cycles. These results illustrate that even within a single, well-constrained laboratory experiment, the dynamics of earthquake nucleation can be highly complex.

Plain Language Summary The fault systems that produce damaging earthquakes are difficult to study directly due to their depth and spatial extent in the Earth's crust. Laboratory earthquake experiments can provide insight into the relevant physical processes active in real earthquake systems. In experiments with granular material that emulates the crushed-up gouge material of real faults, larger labquakes are always preceded by smaller, foreshock events. In this work, we provide a detailed study of the space-time evolution of these microslip foreshocks in one such experiment. We show that even in these simplified analogs of real earthquake cycles, earthquake nucleation processes and frictional behavior can vary dramatically from cycle to cycle. In tectonic fault zones on Earth, such complexity will only be magnified.

1. Introduction

The evolution of stress and strain fields in fault systems plays a fundamental role in earthquake occurrence. Direct observations of these fields are difficult in the real Earth, where the seismogenic zone resides kilometers below the surface. While direct measurements are possible in tectonic fault systems (Hickman & Zoback, 2004; Zoback & Healy, 1992), they are expensive to obtain and provide only pointwise sampling over time scales that are short compared to the full duration of the earthquake cycle.

These difficulties have spawned a plethora of analog laboratory experiments that have for decades played a foundational role in our understanding of fault friction and earthquake physics (Abercrombie & Rice, 2005; Beeler et al., 1994; Marone et al., 1990; Scholz, 1968). A key advantage of laboratory experiments is that the observer controls the driving forces and can closely monitor the system as it approaches failure. In so doing, one can derive basic relations governing fault friction (Dieterich, 1979; Marone, 1998; Ruina, 1983) and study various frictional weakening mechanisms that control the dynamics of large slip events (Beeler et al., 2008; Brodsky & Kanamori, 2001; Goldsby & Tullis, 2011; Rice, 2006; Tisato et al., 2012).

Laboratory earthquake experiments have been performed using a variety of system geometries, and with a diverse array of real rock samples and analog Earth materials. In a typical setup, the loading velocity and normal force are held constant as the system traverses multiple stick-slip cycles of shear motion. Microslip events, apparent in the form of small acoustic emissions, are often observed preceding the failure. These
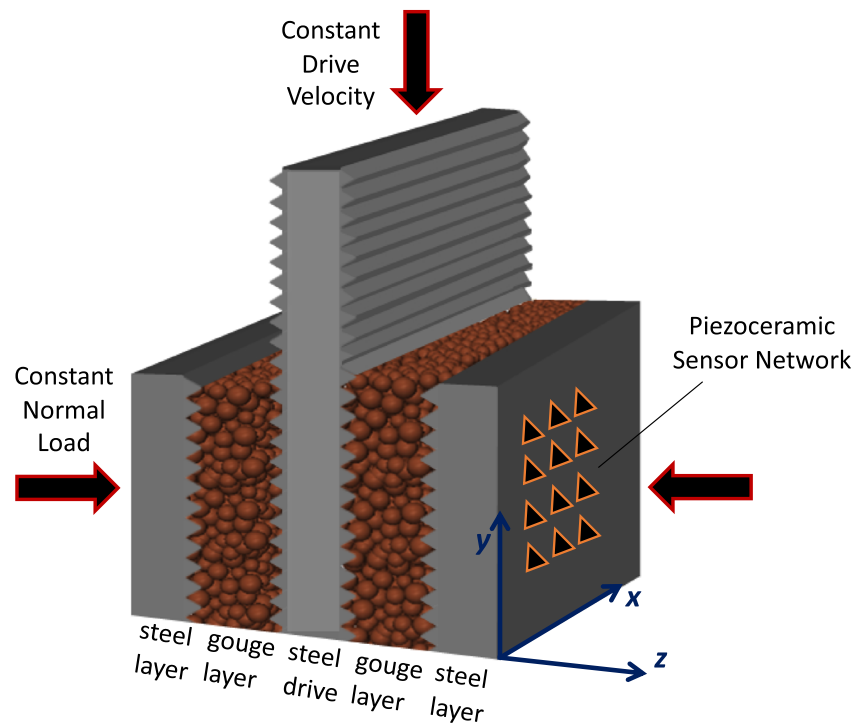
Figure 1. Schematic of the double-direct shear apparatus and sensor geometry (not to scale). This system is driven from the top at constant loading velocity and confined from the sides with constant normal load. Microslip events occur in the gouge layer and are recorded by an array of 12 piezoceramic sensors located outside the steel confining layer. We adopt the (x, y, z) coordinate system shown at the bottom right.

microslip events are not random in their occurrence but instead lend insight into the nucleation process as the system evolves to dynamic rupture (Acosta et al., 2019; Bolton et al., 2019; Brantut et al., 2008; Goebel et al., 2013; Johnson et al., 2013; Lubbers et al., 2018; Main et al., 1989; McLaskey et al., 2014; Passelègue et al., 2013; Rouet-Leduc et al., 2017; Rivière et al., 2018; Scholz, 1968). Studying these events in the laboratory setting may thus help understand their real Earth analogs: the background microseismicity and foreshock sequences that occur between larger, system-spanning ruptures (Abercrombie & Mori, 1996; Chen & Shearer, 2016; Dodge et al., 1996; Ellsworth & Bulut, 2018; Trugman & Ross, 2019).

The focus of this work is on high-resolution spatiotemporal imaging of microslip activity in shear experiments with synthetic fault gouge. While the location of acoustic emission events in intact rock samples or saw cut, block-on-block experiments has become relatively common (David et al., 2018; Goebel et al., 2013; Marty et al., 2019; McLaskey & Glaser, 2011; McLaskey et al., 2010; Thompson et al., 2009), the same cannot be said for granular shear experiments, where the overall frictional behavior and microslip activity may differ substantially. We use state-of-the-art machine learning tools to reliably extract seismic arrivals on multiple sensors and then associate these arrivals to microslip events occurring in the fault gouge layer. With thousands of precisely located events in hand, we study their evolution in space and time within and between individual stick-slip cycles, with an ultimate aim to further our understanding of the physics of the earthquake cycle.

2. Experimental Data

We use experimental data from a double-direct shear (DDS) apparatus developed at Penn State and described previously by a number of research teams (Anthony & Marone, 2005; Johnson et al., 2008; Mair et al., 2007; Rivière et al., 2018; Tinti et al., 2016). This apparatus comprises a central block that is driven at a fixed loading velocity (here 10 µm/s) in analogy to the plate rate in tectonic systems. This loading imparts shear stress within two gouge layers, each of which has lateral dimension 100 mm × 100 mm and an initial thickness of 5 mm. The gouge layers are located on either side of the central driving block and are confined by a second steel layer of 20 mm thickness (Figure 1). In this experiment, the gouge material consists of monodisperse
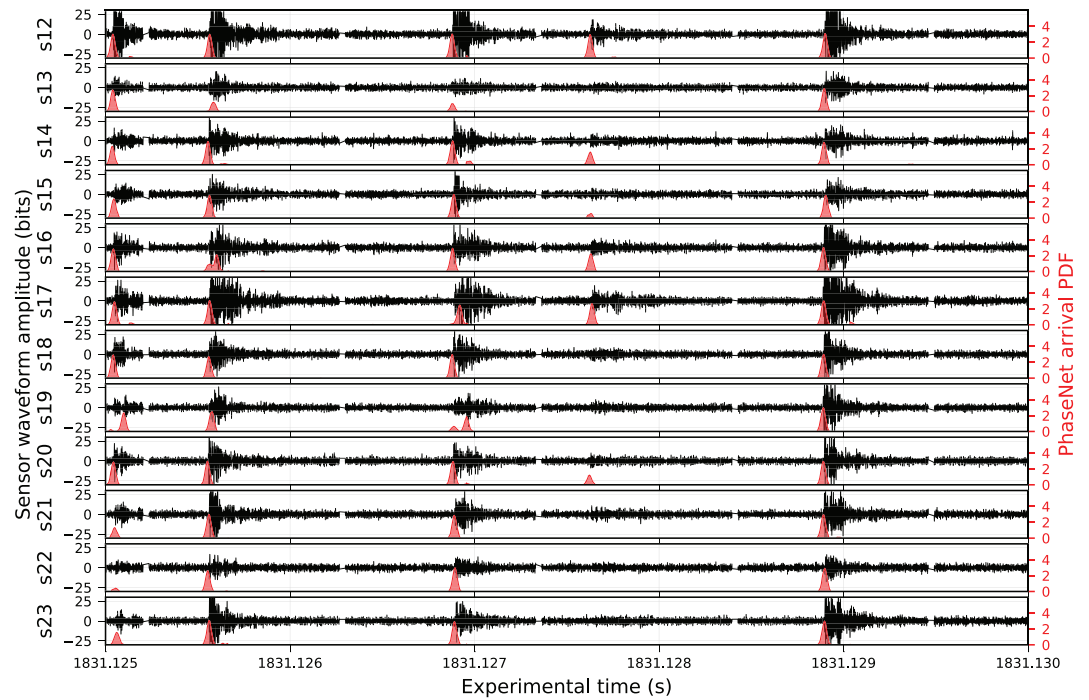
Figure 2. Waveform data and phase detection. Each panel shows a time-aligned 5 ms snapshot of waveform data in experiment p4677 (black lines) at one of the 12 sensors (here numbered 12 through 23). PhaseNet predictions (arrival probabilities) are plotted in red alongside the waveform data, where peaks in the output label function correspond to phase arrivals.

glass beads of 104–149 μm diameter. We use a load-feedback servo control system to maintain a fixed normal stress of 2.5 MPa, while measuring shear stress throughout the experiment.

An important aspect of the experiment is the placement of piezoceramic sensors on the outside of the DDS sample (Figure 1). The sensors are mounted in a steel block at the bottom of blind holes 2 mm from the DDS sample. The sensors are arranged in a matrix with 16.8 mm spacing. Waveform data are recorded continuously for each sensor at ~4 MHz sampling rate. While both gouge layers in the double-direct system are capable of such recordings, we report here on the right layer shown in Figure 1, which has a more complete and regular grid of 12 sensors. This experimental setup was not originally designed to interrogate microslip event locations, so the 12-sensor network covers only a central portion of the gouge layer. As such, we anticipate a limited ability to resolve the locations of microslip activity near the lateral edges of system. However, these events are of less interest here because they are a byproduct of boundary conditions not present in most real Earth fault systems. Future experiments with a more complete array of sensors may however build on these results.

3. Methods

The first step in our analyses is to detect phase arrivals from microslip events on each sensor. To do this, we adapt the PhaseNet detection algorithm of Zhu and Beroza (2019). PhaseNet is a machine learning framework with a classic U-Net architecture that outputs the relative probability of a phase arrival at each time step. Before applying PhaseNet to our data set, we band-pass filter the waveforms into the 0.05–0.8 MHz range that contains the dominant portion of seismic energy from microslip phase arrivals. We constrain the network weights through training on a subset of data with manually reviewed arrivals determined by an energy norm-based picker (McBrearty et al., 2019). After running PhaseNet on the full time series at each sensor, we use a peak-finding algorithm to extract arrival times from the PhaseNet output probabilities (Figure 2). The results are insensitive to the details of the peak-finding algorithm, as in this context PhaseNet provides sharply peaked arrival probabilities.

With the collection of arrival times at each sensor in hand, the next step is to associate the arrivals with individual events. This process is simplified by the fact that moveout of arrivals across the sensor network
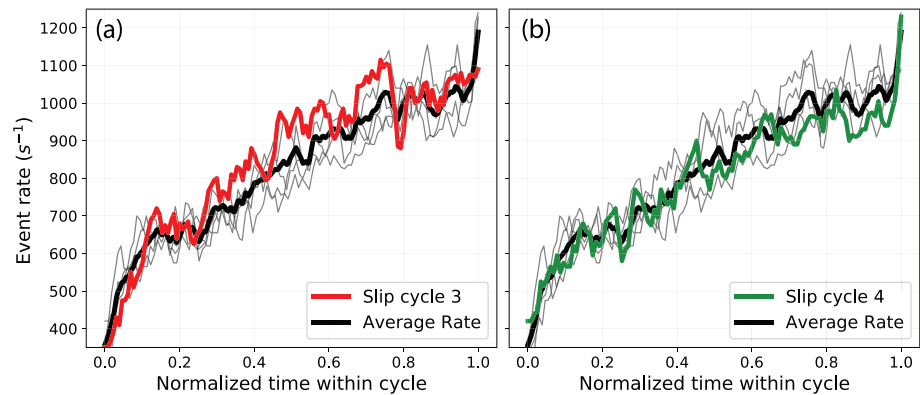
Figure 3. Comparison of microslip event rates in stick-slip Cycles 3 and 4. Event rates are plotted as a function of normalized time within the slip event (bounded from 0 to 1) and compared to the other stick-slip cycles (gray) and the average rate across cycles (black).

is typically much shorter than the interevent times (typical interevent times are ~1 ms, see Figure S1 in the supporting information). Because of this, there are relatively few overlapping events (an observation confirmed with visual inspection of the waveforms), and thus, applying a temporal clustering algorithm, DBSCAN (Ester et al., 1996), is sufficient to group sets of arrivals into events. We define an event to consist of four or more arrivals within a time window of 35 μs, where the latter threshold is guided by the maximum possible moveout lag across the sensor network. This requirement of four or more arrivals reduces the risk for local sensor noise to generate a false event but may exclude some of the smallest microslip events from our final catalog.

Our ultimate goal is to provide locations of the microslip events that generate the detected phase arrivals. This final step is more difficult than it may appear at first glance due to physical and geometric constraints. Since the wave speed in the steel block containing the sensors (~3,250 m/s) is much larger than that of the fault gouge (~570 m/s; e.g., Domenico, 1977; Muqtadir et al., 2020), ray theoretical arguments imply that any ray arriving at one of the sensors must have been traveling near vertically in the gouge layer, as the critical angle from gouge to steel is of order 10°. This constraint accentuates the traditional tradeoff between event depth and origin time to the extent that we have essentially zero depth resolution in the gouge. Consequently, we resolve and report only the lateral (x, y) coordinates of each event within the gouge layer.

The phase arrivals we are working with are too numerous (tens of thousands per sensor) to manually review more than a few for quality control purposes. Because of this, our location algorithm must account for the possibility of one or more outlier arrival times within each event, which precludes traditional location approaches based on L2 norm residual minimization. With this in mind, we combine a grid search in x and y with a robust optimization approach based on the RAndom SAmpling Consensus (RANSAC) algorithm (Fischler & Bolles, 1981) to minimize the misfit between the observed and predicted arrival times, the latter being determined through ray tracing. The RANSAC method has been used by statisticians for several decades in regression problems with an unknown number of outlier data points but has only recently been adopted by the seismology community (Woollam et al., 2020; Zhu et al., 2017). To our knowledge, this is the first application of RANSAC to the study of microslip events in laboratory earthquake experiments. The RANSAC method is quite effective for our purposes, where in some instances even the suppression of a single outlier data point can dramatically improve the location (Figure S2). Because the phase type of the detected arrivals was unknown a priori, we initially located using both P wave and S wave velocity models. However, we found that the S wave locations gave systematically lower misfits in the vast majority of instances, and hence, our location results assume S wave arrivals. This is consistent with the association of acoustic emissions with the rearrangement of force chains that impart shear couples on the gouge formation (Anthony & Marone, 2005; Gao et al., 2019).

4. Results

We examine microslip event rates and locations within five stick-slip cycles during experiment p4677. Microslip events occur at all times, indicating that the fault never fully locks (Scuderi et al., 2015). Event
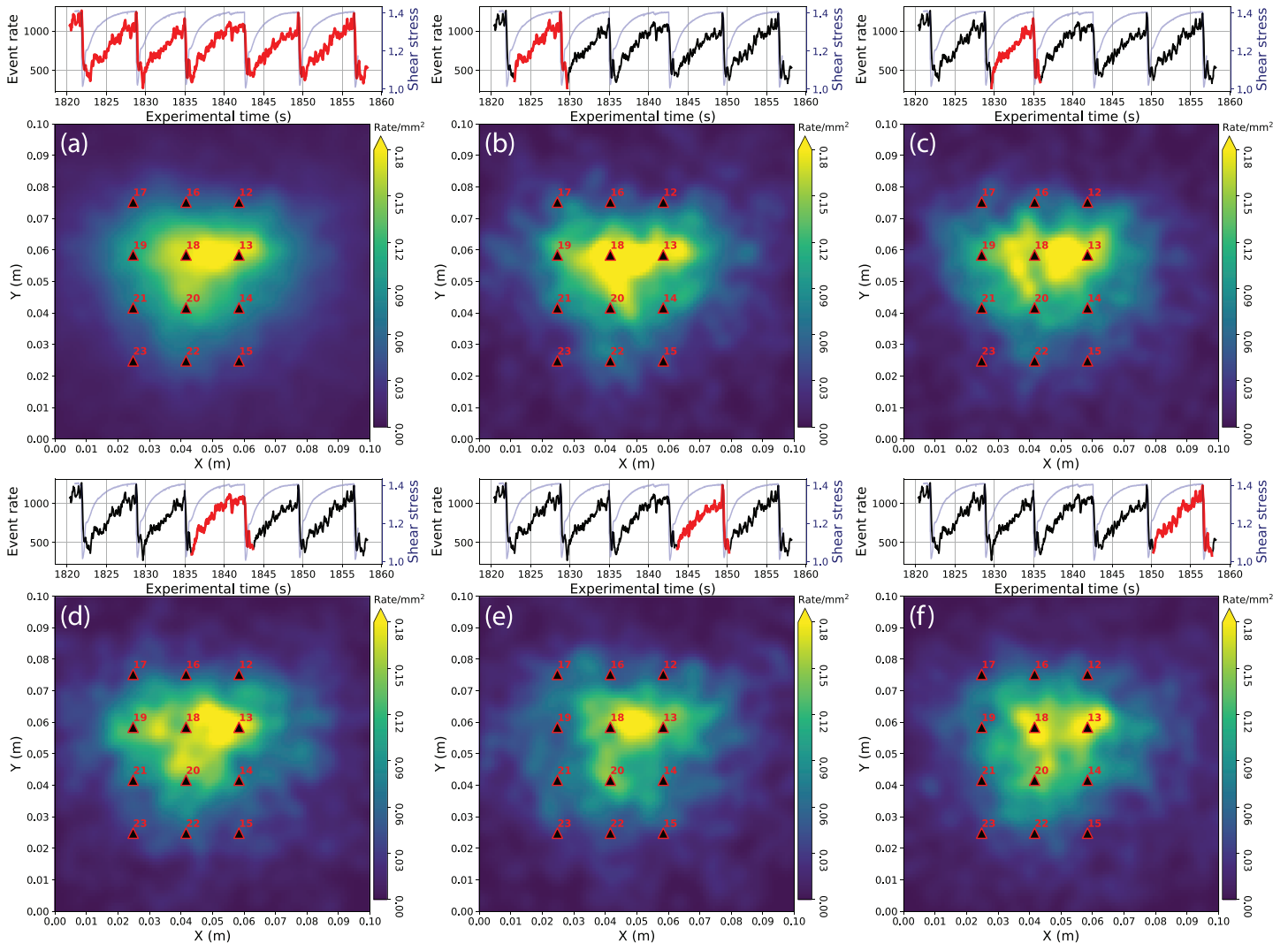
Figure 4. Comparison of microslip activity during the five stick-slip cycles analyzed in this study. Panel (a) shows the results for the experiment as a whole, while panels (b) through (f) show results for each individual cycle. The top plot in each panel contains an event rate time series (black) plotted alongside the measured shear stress (light blue). The bottom plot shows a kernel density estimate representation of the spatial distribution of microslip activity in the (x, y) plane, with warmer colors indicating higher event rates per unit area. Here, we use a Gaussian kernel width of 2.5 mm, in line with typical location uncertainties.

rates increase during each slip cycle in tandem with shear stress, though the details of this time evolution vary between cycles. This variability is most clearly observed by comparing the time evolution of microslip event rates (here calculated in sliding windows of 0.2 s duration) within individual stick-slip cycles to the average trend across all cycles (Figures 3 and S3). The third stick-slip event, for example, features higher-than-average event rates throughout the cycle and no systematic increase near failure, while the fourth follows the general trend of the remaining stick-slip cycles before culminating in a prominent spike in microslip activity immediately preceding failure.

The essential contribution of this work is constraining the locations of these microslip events; previous works have documented the decrease in seismic b value leading to failure (Goebel et al., 2013, 2017; Main et al., 1989; Rivière et al., 2018; Sammonds et al., 1992; Scholz, 1968; Weeks et al., 1978). Our location approach uses a five-sample RANSAC implementation with a tolerance level of 5 μs, which is comparable to the uncertainty in the PhaseNet predictions. Under these conditions, we are able to locate slightly more than half (15,222) of the 30,326 total detected events. The different stick-slip cycles in our experiment share some universal features, most notably that the microslip event activity concentrates near the center of the system (between sensors 18, 13, 20, and 14). This may indicate a correspondence between microslip activity
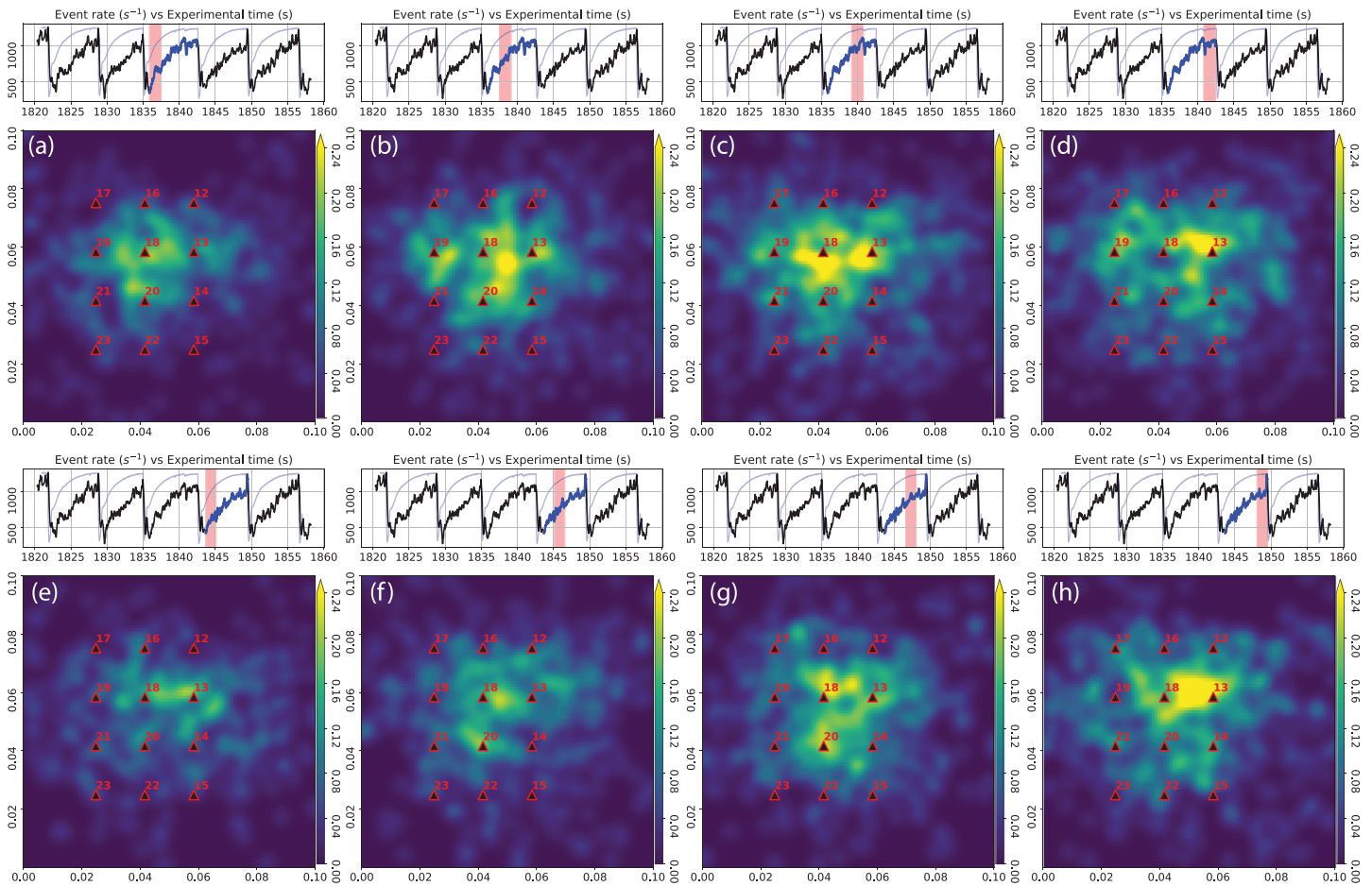
Figure 5. Space-time evolution of microslip activity during the third and fourth stick-slip cycles in the experiment (panels a–d and e–h, respectively). As in Figure 4, each panel contains a spatial density map of microslip activity during one quarter of the slip cycle (time period marked in red).

and the area of the fault plane where the breakage and rearrangements of force chains spanning the gouge layer are most prevalent (Anthony & Marone, 2005; Daniels & Hayman, 2008; Gao et al., 2019). Although our sensor network does not encompass the entire slip plane, it covers a broad enough area that it is unlikely that the central concentration is simply an artifact of station geometry.

While the spatial patterns averaged over multiple cycles appear rather simple (Figure 4a), each stick-slip cycle exhibits a unique spatiotemporal signature that traces out a distinctive pattern of microslip event activity. Figure 5 illustrates this by taking snapshots of microslip activity at different points in the third and fourth stick-slip cycles highlighted above (see Figure S4 for the other slip events). During the third stick-slip cycle, microslip event activity achieves a high rate relatively early on, and there are multiple spatial and temporal peaks in event rate before the final stick-slip failure. This behavior is likely related to the notch in the shear stress curve at ~1,841 s, where a small stick-slip event is embedded in the full stick-slip cycle. The fourth stick-slip cycle, in contrast, features a steady climb in event rate and a distinct, localized hot spot in microslip activity during the final stages of the nucleation process.

We can quantify these spatiotemporal relations with the Kullback-Leibler (KL) divergence metric (Kullback & Leibler, 1951), which is commonly used to compare two probability distributions (MacKay & Kay, 2003). Here, we use a symmetric definition of the KL divergence, appropriate for cases when there is no reference probability distribution. Lower values of KL divergence indicate a higher degree of similarity in the two distributions, approaching 0 in the limit that the distributions are identical. To apply this concept to the microslip event data, we divide each stick-slip cycle into 20 nonoverlapping time windows (100 time windows in total across the five stick-slip cycles). For each time window, we compute a spatial probability
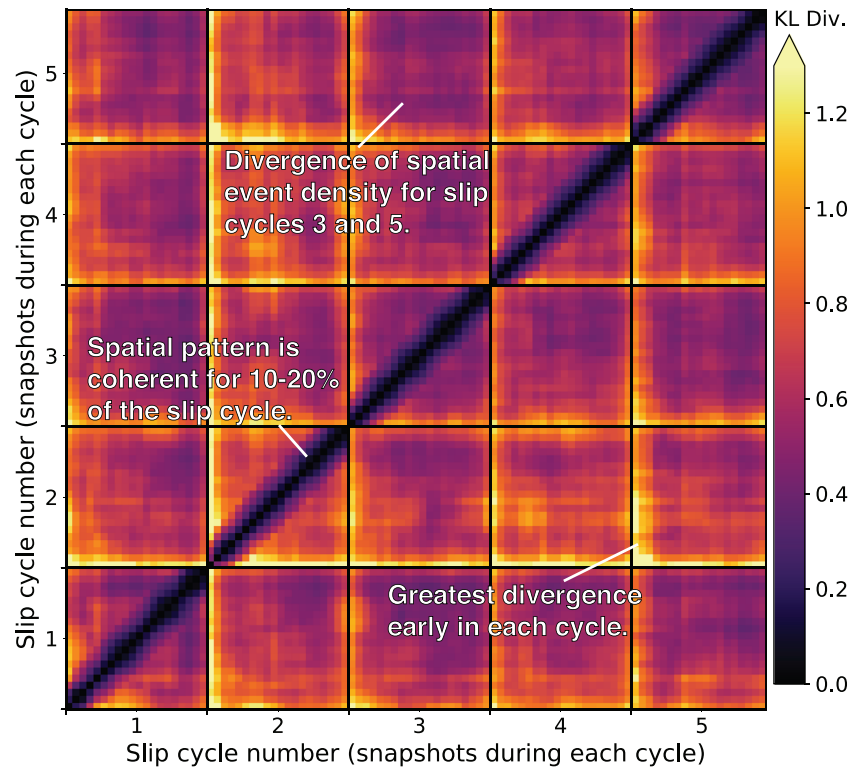
Figure 6. Symmetric KL divergence between different snapshots in time of microslip event activity. The large grid cells along the *x* and *y* axes correspond to different stick-slip cycles, labeled 1 to 5. Each cycle is discretized into 20 time windows, and the pairwise KL divergence of the spatial event density in that time window with event density in all other time windows is displayed in matrix form. In this way, our analysis explores all possible combinations of snapshots within pairs of cycles. Darker colors correspond to lower values of KL divergence, and hence more similar spatial event densities.

density map of microslip activity (like those shown in Figures 4 and 5) and calculate the KL divergence of these spatial density maps with those from all other time windows.

The results of this analysis are presented in Figure 6 and lead to three main observations. First, the width of the diagonal streak in the KL matrix suggests that the spatial patterns of microslip activity are temporally persistent only for about 10–20% of the stick-slip cycle before this similarity begins to deteriorate. Second, the spatial distributions for different stick-slip cycles (represented in the off-diagonal square grids) share some similar features, notably the concentration of microslip activity near the center of the apparatus, but are measurably divergent in their fine-scale details. Third, in comparing different stick-slip cycles, the spatial patterns are most dissimilar at the beginning of the cycle, where the microslip activity is effectively randomized in the aftermath of the previous stick-slip event.

5. Discussion and Conclusions

In this study, we analyze the spatial and temporal progression of microslip activity in a DDS experiment with synthetic fault gouge. Our processing workflow uses waveform data from an array of 12 piezoceramic sensors in combination with machine learning seismological techniques to detect, associate, and locate microslip events within the gouge layer. The individual stick-slip cycles in our experiment share some universal characteristics, including an increase in microslip event rate as stick-slip failure approaches and a spatial concentration of these events near the center of the apparatus. However, we also find a diversity of microslip spatiotemporal patterns across stick-slip cycles and provide quantitative support for these observations through KL divergence calculations. Our results suggest that each stick-slip cycle comprises a unique spatiotemporal evolution of microslip activity as failure approaches and that the support of shear stress is inhomogeneously distributed across the gouge layer. While event rates tend to increase later in the slip cycle,

the progression is not always smooth, and the final instances preceding failure may feature multiple hot spots of concentrated microslip activity.

This is a very different picture than the classic paradigm of earthquake nucleation as a smooth expansion of localized aseismic slip until a critical dimension is reached and dynamic rupture initiates (Ohnaka, 2000). Preslip nucleation models of this type are often contrasted (Mignan, 2014) with those corresponding to an earthquake cascade, where individual foreshock events trigger one another and eventually the mainshock as part of a stochastic process. Our observations do not fit neatly into either end-member model, as we see evidence both of stochastic triggering behavior and a systematic acceleration of microslip activity as failure approaches. Hybrid models are more appealing (McLaskey, 2019), but even they are prone to oversimplify the underlying physics.

With these new results in hand, it is important to bear in mind their limitations. Laboratory earthquake experiments are imperfect analogs for real Earth fault systems. We focused on an experiment that features a gouge layer like those present in the real Earth and thus shares some of the same important underlying physics. Nevertheless, this experiment is highly simplified and does not include elevated temperature, the geological or geometrical heterogeneity of real fault zones, the influence of fluid transport, or the interaction of adjacent fault systems.

Because of this, it is uncertain how well the conclusions we derive here will generalize and scale to rupture characteristics of real earthquakes. However, it is worth considering that even within the context of a single experiment, we observe a rich complexity in rupture nucleation replete with significant cycle-to-cycle variability. The granular physics of fault gouge may thus significantly complicate nucleation and failure. The implications of this are self-evident, as it is hard to imagine things getting simpler in the real Earth.

Data Availability Statement

Experimental data for run p4677 are publicly available in the repository (at https://zenodo.org/record/3981051#.XzQiRJNKjLg).

References

Abercrombie, R. E., & Mori, J. (1996). Occurrence patterns of foreshocks to large earthquakes in the western United States. *Nature*, *381*(6580), 303–307. https://doi.org/10.1038/381303a0

Abercrombie, R. E., & Rice, J. R. (2005). Can observations of earthquake scaling constrain slip weakening? *Geophysical Journal International*, *162*(2), 406–424. https://doi.org/10.1111/j.1365-246X.2005.02579.x

Acosta, M., Passelègue, F. X., Schubnel, A., Madariaga, R., & Violay, M. (2019). Can precursory moment release scale with earthquake magnitude? A view from the laboratory. *Geophysical Research Letters*, *46*, 12,927–12,937. https://doi.org/10.1029/2019GL084744

Anthony, J. L., & Marone, C. (2005). Influence of particle characteristics on granular friction. *Journal of Geophysical Research*, *110*, B08409. https://doi.org/10.1029/2004JB003399

Beeler, N. M., Tullis, T. E., & Goldsby, D. L. (2008). Constitutive relationships and physical basis of fault strength due to flash heating. *Journal of Geophysical Research*, *113*, B01401. https://doi.org/10.1029/2007JB004988

Beeler, N. M., Tullis, T. E., & Weeks, J. D. (1994). The roles of time and displacement in the evolution effect in rock friction. *Geophysical Research Letters*, *21*(18), 1987–1990. https://doi.org/10.1029/94GL01599

Bolton, D. C., Shokouhi, P., Rouet-Leduc, B., Hulbert, C., Rivière, J., Marone, C., & Johnson, P. A. (2019). Characterizing acoustic signals and searching for precursors during the laboratory seismic cycle using unsupervised machine learning. *Seismological Research Letters*, *90*(3), 1088–1098. https://doi.org/10.1785/0220180367

Brantut, N., Schubnel, A., Rouzaud, J.-N., Brunet, F., & Shimamoto, T. (2008). High-Velocity frictional properties of a clay-bearing fault gouge and implications for earthquake mechanics. *Journal of Geophysical Research*, *113*, B10401. https://doi.org/10.1029/2007JB005551

Brodsky, E. E., & Kanamori, H. (2001). Elastohydrodynamic lubrication of faults. *Journal of Geophysical Research*, *106*(B8), 16,357–16,374. https://doi.org/10.1029/2001JB000430

Chen, X., & Shearer, P. M. (2016). Analysis of foreshock sequences in California and implications for earthquake triggering. *Pure and Applied Geophysics*, *173*(1), 133–152. https://doi.org/10.1007/s00024-015-1103-0

Daniels, K. E., & Hayman, N. W. (2008). Force chains in seismogenic faults visualized with photoelastic granular shear experiments. *Journal of Geophysical Research*, *113*, B11411. https://doi.org/10.1029/2008JB005781

David, E. C., Brantut, N., Hansen, L. N., & Mitchell, T. M. (2018). Absence of stress-induced anisotropy during brittle deformation in antigorite serpentinite. *Journal of Geophysical Research: Solid Earth*, *123*, 10,616–10,644. https://doi.org/10.1029/2018JB016255

Dieterich, J. H. (1979). Modeling of rock friction: 1. Experimental results and constitutive equations. *Journal of Geophysical Research*, *84*(B5), 2161–2168. https://doi.org/10.1029/JB084iB05p02161

Dodge, D. A., Beroza, G. C., & Ellsworth, W. L. (1996). Detailed observations of California foreshock sequences: Implications for the earthquake initiation process. *Journal of Geophysical Research*, *101*(B10), 22,371–22,392. https://doi.org/10.1029/96JB02269

Domenico, S. N. (1977). Elastic properties of unconsolidated porous sand reservoirs. *Geophysics*, *42*(7), 1339–1368. https://doi.org/10.1190/1.1440797

Ellsworth, W. L., & Bulut, F. (2018). Nucleation of the 1999 Izmit earthquake by a triggered cascade of foreshocks. *Nature Geoscience*, *11*, 531–535. https://doi.org/10.1038/s41561-018-0145-1

Ester, M., Kriegel, H.-P., Sander, J., & Xu, X. (1996). A density-based algorithm for discovering clusters in large spatial databases with noise. In *Proceedings of the Second International Conference on Knowledge Discovery and Data Mining* (Vol. *96*, pp. 226–231), Portland, OR: AAAI Press.

Fischler, M. A., & Bolles, R. C. (1981). Random sample consensus: A paradigm for model fitting with applications to image analysis and automated cartography.

Gao, K., Guyer, R., Rougier, E., Ren, C. X., & Johnson, P. A. (2019). From stress chains to acoustic emission. *Physical Review Letters*, *123*(4), 048003. https://doi.org/10.1103/PhysRevLett.123.048003

Goebel, T. H. W., Kwiatek, G., Becker, T. W., Brodsky, E. E., & Dresen, G. (2017). What allows seismic events to grow big? Insights from b-value and fault roughness analysis in laboratory stick-slip experiments. *Geology*, *45*(9), 815–818. https://doi.org/10.1130/G39147.1

Goebel, T. H. W., Schorlemmer, D., Becker, T. W., Dresen, G., & Sammis, C. G. (2013). Acoustic emissions document stress changes over many seismic cycles in stick-slip experiments. *Geophysical Research Letters*, *40*, 2049–2054. https://doi.org/10.1002/grl.50507

Goldsby, D. L., & Tullis, T. E. (2011). Flash heating leads to low frictional strength of crustal rocks at earthquake slip rates. *Science*, *334*(6053), 216–218. https://doi.org/10.1126/science.1207902

Hickman, S., & Zoback, M. (2004). Stress orientations and magnitudes in the SAFOD pilot hole. *Geophysical Research Letters*, *31*, L15S12. https://doi.org/10.1029/2004GL020043

Johnson, P. A., Ferdowsi, B., Kaproth, B. M., Scuderi, M., Griffa, M., Carmeliet, J., et al. (2013). Acoustic emission and microslip precursors to stick-slip failure in sheared granular material. *Geophysical Research Letters*, *40*, 5627–5631. https://doi.org/10.1002/2013GL057848

Johnson, P. A., Savage, H., Knuth, M., Gomberg, J., & Marone, C. (2008). Effects of acoustic waves on stick–slip in granular media and implications for earthquakes. *Nature*, *451*(7174), 57–60. https://doi.org/10.1038/nature06440

Kullback, S., & Leibler, R. A. (1951). On information and sufficiency. *Annals of Mathematical Statistics*, *22*(1), 79–86 EN. https://doi.org/10.1214/aoms/1177729694

Lubbers, N., Bolton, D. C., Mohd-Yusof, J., Marone, C., Barros, K., & Johnson, P. A. (2018). Earthquake catalog-based machine learning identification of laboratory fault states and the effects of magnitude of completeness. *Geophysical Research Letters*, *45*, 13,269–13,276. https://doi.org/10.1029/2018GL079712

MacKay, D. J. C., & Kay, D. J. C. M. (2003). *Information theory, inference and learning algorithms*. Cambridge, UK: Cambridge University Press.

Main, I. G., Meredith, P. G., & Jones, C. (1989). A reinterpretation of the precursory seismic B-value anomaly from fracture mechanics. *Geophysical Journal International*, *96*(1), 131–138. https://doi.org/10.1111/j.1365-246X.1989.tb05255.x

Mair, K., Marone, C., & Young, R. P. (2007). Rate dependence of acoustic emissions generated during shear of simulated fault gouge. *Bulletin of the Seismological Society of America*, *97*(6), 1841–1849. https://doi.org/10.1785/0120060242

Marone, C. (1998). Laboratory-derived friction laws and their application to seismic faulting. *Annual Review of Earth and Planetary Sciences*, *26*(1), 643–696. https://doi.org/10.1146/annurev.earth.26.1.643

Marone, C., Raleigh, C. B., & Scholz, C. H. (1990). Frictional behavior and constitutive modeling of simulated fault gouge. *Journal of Geophysical Research*, *95*(B5), 7007–7025. https://doi.org/10.1029/JB095iB05p07007

Marty, S., Passelègue, F. X., Aubry, J., Bhat, H. S., Schubnel, A., & Madariaga, R. (2019). Origin of high-frequency radiation during laboratory earthquakes. *Geophysical Research Letters*, *46*, 3755–3763. https://doi.org/10.1029/2018GL080519

McBrearty, I. W., Gomberg, J., Delorey, A. A., & Johnson, P. A. (2019). Earthquake arrival association with backprojection and graph theory. *Bulletin of the Seismological Society of America*, *109*(6), 2510–2531. https://doi.org/10.1785/0120190081

McLaskey, G. C. (2019). Earthquake initiation from laboratory observations and implications for foreshocks. *Journal of Geophysical Research: Solid Earth*, *124*, 12,882–12,904. https://doi.org/10.1029/2019JB018363

McLaskey, G. C., & Glaser, S. D. (2011). Micromechanics of asperity rupture during laboratory stick slip experiments. *Geophysical Research Letters*, *38*, L12302. https://doi.org/10.1029/2011GL047507

McLaskey, G. C., Glaser, S. D., & Grosse, C. U. (2010). Beamforming array techniques for acoustic emission monitoring of large concrete structures. *Journal of Sound and Vibration*, *329*(12), 2384–2394. https://doi.org/10.1016/j.jsv.2009.08.037

McLaskey, G. C., Kilgore, B. D., Lockner, D. A., & Beeler, N. M. (2014). Laboratory generated M-6 earthquakes. *Pure and Applied Geophysics*, *171*(10), 2601–2615. https://doi.org/10.1007/s00024-013-0772-9

Mignan, A. (2014). The debate on the prognostic value of earthquake foreshocks: A meta-analysis. *Scientific Reports*, *4*, 4099. https://doi.org/10.1038/srep04099

Muqtadir, A., Al-Dughaimi, S., & Dvorkin, J. (2020). Deformation of granular aggregates: Static and dynamic bulk moduli. *Journal of Geophysical Research: Solid Earth*, *125*, e2019JB018604. https://doi.org/10.1029/2019JB018604

Ohnaka, M. (2000). A physical scaling relation between the size of an earthquake and its nucleation zone size. *Pure and Applied Geophysics*, *157*(11), 2259–2282. https://doi.org/10.1007/PL00001084

Passelègue, F. X., Schubnel, A., Nielsen, S., Bhat, H. S., & Madariaga, R. (2013). From sub-Rayleigh to supershear ruptures during stick-slip experiments on crustal rocks. *Science*, *340*(6137), 1208–1211. https://doi.org/10.1126/science.1235637

Rice, J. R. (2006). Heating and weakening of faults during earthquake slip. *Journal of Geophysical Research*, *111*, B05311. https://doi.org/10.1029/2005JB004006

Rivière, J., Lv, Z., Johnson, P. A., & Marone, C. (2018). Evolution of B-value during the seismic cycle: Insights from laboratory experiments on simulated faults. *Earth and Planetary Science Letters*, *482*, 407–413. https://doi.org/10.1016/j.epsl.2017.11.036

Rouet-Leduc, B., Hulbert, C., Lubbers, N., Barros, K., Humphreys, C. J., & Johnson, P. A. (2017). Machine learning predicts laboratory earthquakes. *Geophysical Research Letters*, *44*, 2017GL074677. https://doi.org/10.1002/2017GL074677

Ruina, A. (1983). Slip instability and state variable friction laws. *Journal of Geophysical Research*, *88*(B12), 10359. https://doi.org/10.1029/JB088iB12p10359

Sammonds, P. R., Meredith, P. G., & Main, I. G. (1992). Role of pore fluids in the generation of seismic precursors to shear fracture. *Nature*, *359*(6392), 228–230. https://doi.org/10.1038/359228a0

Scholz, C. H. (1968). The frequency-magnitude relation of microfracturing in rock and its relation to earthquakes. *Bulletin of the Seismological Society of America*, *58*(1), 399–415.

Scuderi, M. M., Carpenter, B. M., Johnson, P. A., & Marone, C. (2015). Poromechanics of stick-slip frictional sliding and strength recovery on tectonic faults. *Journal of Geophysical Research: Solid Earth*, *120*, 6895–6912. https://doi.org/10.1002/2015JB011983

Thompson, B. D., Young, R. P., & Lockner, D. A. (2009). Premonitory acoustic emissions and stick-slip in natural and smooth-faulted westerly granite. *Journal of Geophysical Research*, *114*, B02205. https://doi.org/10.1029/2008JB005753

Tinti, E., Scuderi, M. M., Scognamiglio, L., Stefano, G. D., Marone, C., & Collettini, C. (2016). On the evolution of elastic properties during laboratory stick-slip experiments spanning the transition from slow slip to dynamic rupture. *Journal of Geophysical Research: Solid Earth*, *121*, 8569–8594. https://doi.org/10.1002/2016JB013545

Tisato, N., Di Toro, G., De Rossi, N., Quaresimin, M., & Candela, T. (2012). Experimental investigation of flash weakening in limestone. *Journal of Structural Geology*, *38*, 183–199. https://doi.org/10.1016/j.jsg.2011.11.017

Trugman, D. T., & Ross, Z. E. (2019). Pervasive foreshock activity across Southern California. *Geophysical Research Letters*, *46*, 8772–8781. https://doi.org/10.1029/2019GL083725

Weeks, J., Lockner, D., & Byerlee, J. (1978). Change in B-values during movement on cut surfaces in granite. *Bulletin of the Seismological Society of America*, *68*(2), 333–341.

Woollam, J., Rietbrock, A., Leitloff, J. & Hinz, S. (2020). HEX: Hyperbolic Event eXtractor, a Seismic Phase Associator for Highly Active Seismic Regions. *Seismological Research Letters*. https://doi.org/10.1785/0220200037

Zhu, W., & Beroza, G. C. (2019). PhaseNet: A deep-neural-network-based seismic arrival-time picking method. *Geophysical Journal International*, *216*(1), 261–273. https://doi.org/10.1093/gji/ggy423

Zhu, L., Liu, E., McClellan, J., Zhao, Y., Li, W., Li, Z., & Peng, Z. (2017). Estimation of passive microseismic event location using random sampling-based curve fitting. *SEG technical program expanded abstracts 2017* (pp. 2791–2796). Society of Exploration Geophysicists. https://doi.org/10.1190/segam2017-17730445.1

Zoback, M. D., & Healy, J. H. (1992). In situ stress measurements to 3.5 km depth in the Cajon Pass Scientific Research Borehole: Implications for the mechanics of crustal faulting. *Journal of Geophysical Research*, *97*(B4), 5039–5057. https://doi.org/10.1029/91JB02175

Supporting Information for "The Spatio-temporal Evolution of Granular Microslip Precursors to Laboratory Earthquakes"

Daniel T. Trugman[1,2], Ian W. McBrearty[3], David C. Bolton[4,5], Robert A.

Guyer[2,6], Chris Marone[4,5], Paul A. Johnson[2]

[1]Department of Geological Sciences, Jackson School of Geosciences, The University of Texas at Austin

[2]Geophysics Group, Earth and Environmental Sciences Division, Los Alamos National Laboratory

[3]Department of Geophysics, Stanford University

[4]Department of Geosciences, Pennsylvania State University

[5]Dipartimento Scienze della Terra, Sapienza Università di Roma, Italy

[6]Department of Physics, University of Nevada, Reno

Contents of this file

June 4, 2020, 3:59pm

Introduction

This supplementary material contains several figures that support the results presented in the main text. Figure S1 shows the distribution of microslip inter-event times. Figure S2 compares event location using the traditional L2 residual norm approach to the RANSAC approach deployed in this study. Figure S3 compares microslip event rates for different slip cycles. Figure S4 compares spatial event density maps for different time windows.
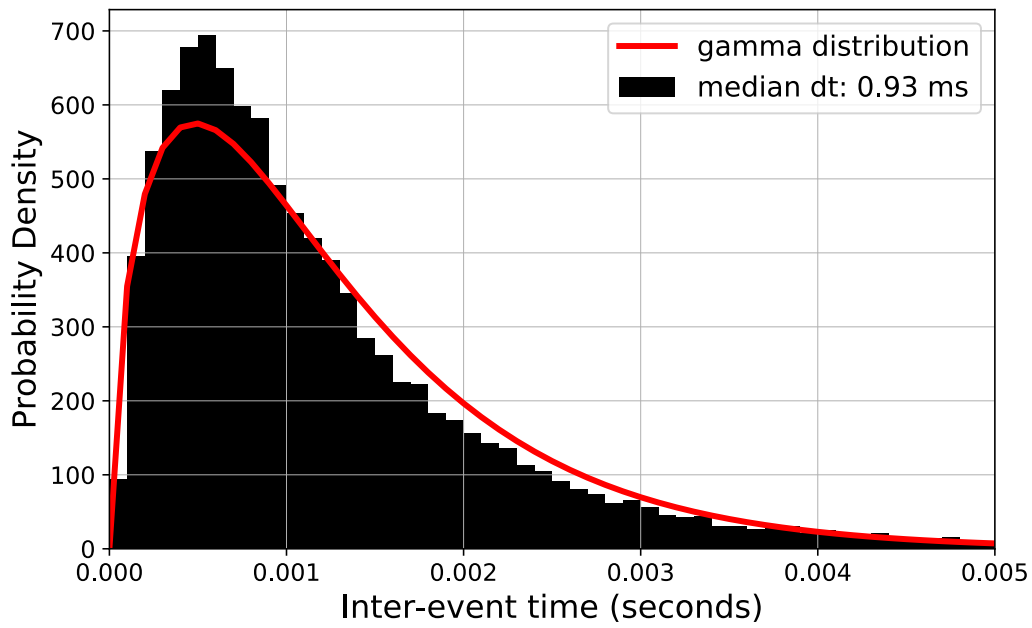
Figure S1. Probability distribution of inter-event times for the microslip event catalog. The median value is 0.93 ms.
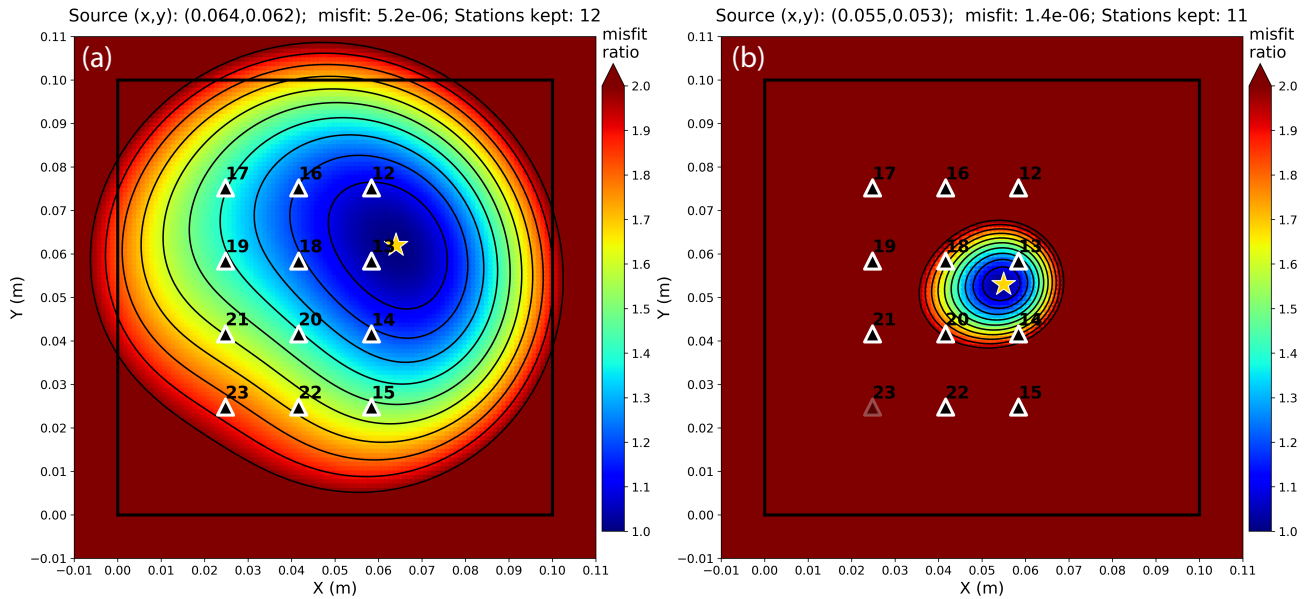
Figure S2. Illustration of the RANSAC event location approach. Each panel shows the misfit between the observed and predicted arrivals for a single microslip event. Panel (a) corresponds to the results using a conventional L2-norm based inversion approach, while panel (b) corresponds to the results using RANSAC for outlier removal. Predicted arrival times are evaluated via grid search over source locations, with spacing of 0.001m for each point in the domain $0 \leq (x, y) \leq 0.1$ m, and with a padding region outside these bounds to mitigate edge artifacts. The colorscale is a measure of relative misfit: the ratio between the misfit at a given grid point and that at its minimum (the inferred hypocenter), marked with a star. The RANSAC approach detects and removes a single outlier sensor (s23, shaded in panel b), thus providing a lower RMS misfit (1.4e μs compared to 5.2 μs) and better spatial resolution (the tightness of misfit contours).
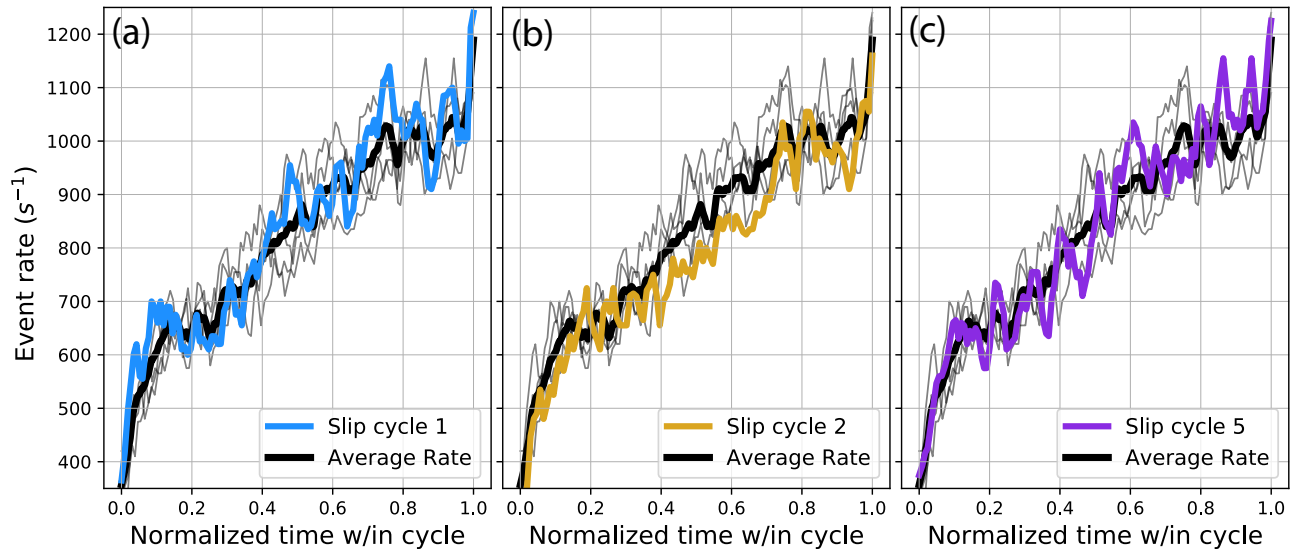
Figure S3. Comparison of microslip event rates in stick-slip cycles one, two, and five. See main text for cycles three and four. Event rates are plotted as a function of normalized time within the slip event (bounded from 0 to 1), and compared to the average rate across cycles (black).
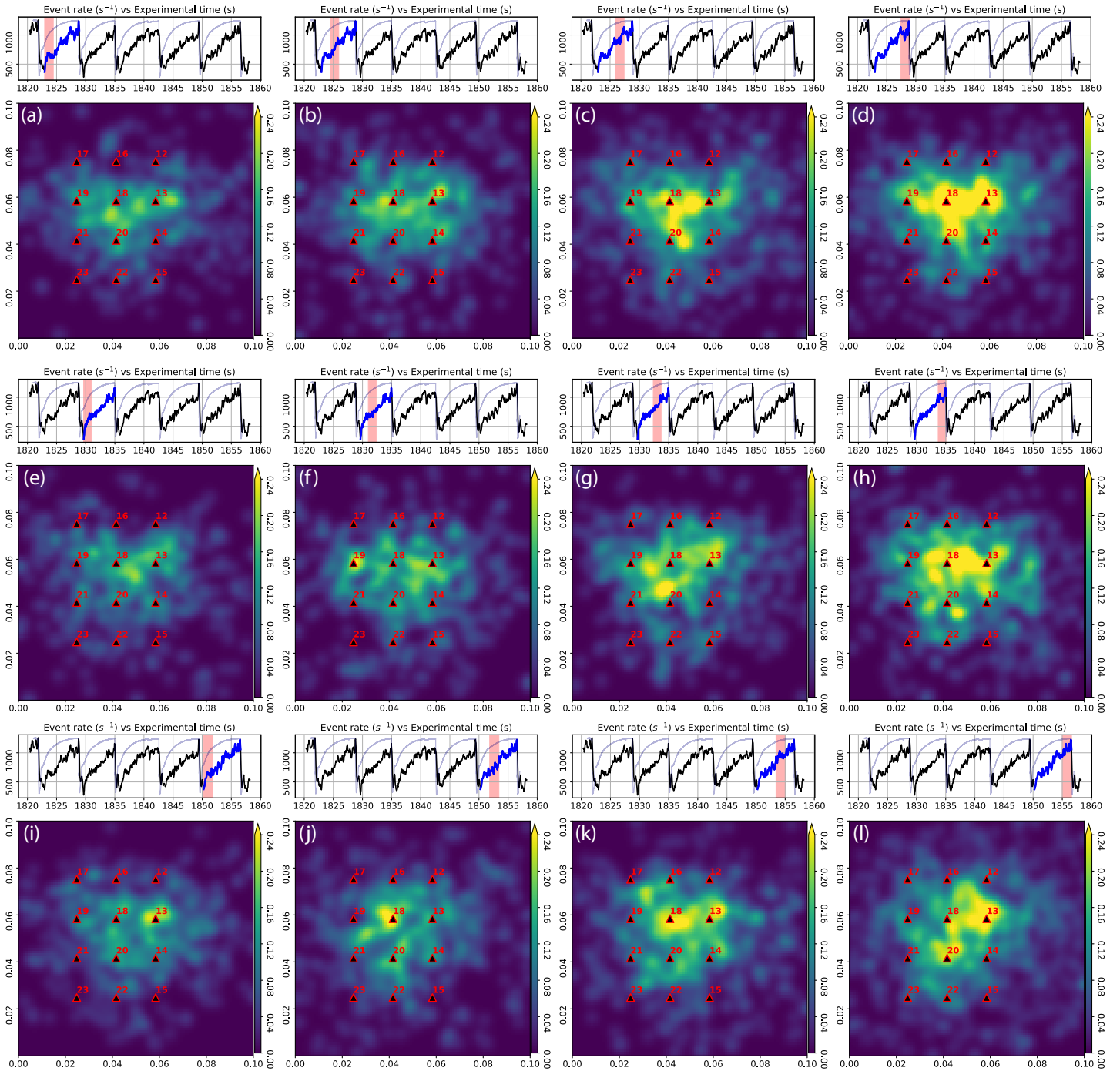
Figure S4. Space-time evolution of microslip activity during the first, second and fifth stick-slip cycles in the experiment (panels a–d, e–h, i–l, respectively). See main text for cycles three and four. Each panel contains a spatial map of microslip activity during one quarter of the slip cycle (time period marked in red). Warmer colors in the spatial map indicate higher event rates per unit area.

June 4, 2020, 3:59pm